

Buoyancy-driven instabilities of miscible two-layer stratifications in porous media and Hele-Shaw cells

P. M. J. TREVELYAN, C. ALMARCHA AND A. DE WIT†

Nonlinear Physical Chemistry Unit, Center for Nonlinear Phenomena and Complex Systems,
Faculté des Sciences, Université Libre de Bruxelles (ULB), CP 231, 1050 Brussels, Belgium

(Received 2 April 2010; revised 6 September 2010; accepted 21 September 2010;
first published online 31 January 2011)

Buoyancy-driven instabilities of a horizontal interface between two miscible solutions in the gravity field are theoretically studied in porous media and Hele-Shaw cells (two glass plates separated by a thin gap). Beyond the classical Rayleigh–Taylor (RT) and double diffusive (DD) instabilities that can affect such two-layer stratifications right at the initial time of contact, diffusive-layer convection (DLC) as well as delayed-double diffusive (DDD) instabilities can set in at a later time when differential diffusion effects act upon the evolving density profile starting from an initial step-function profile between the two miscible solutions. The conditions for these instabilities to occur can therefore be obtained only by considering time evolving base-state profiles. To do so, we perform a linear stability analysis based on a quasi-steady-state approximation (QSSA) as well as nonlinear simulations of a diffusion–convection model to classify and analyse all possible buoyancy-driven instabilities of a stratification of a solution of a given solute A on top of another miscible solution of a species B. Our theoretical model couples Darcy’s law to evolution equations for the concentration of species A and B ruling the density of the miscible solutions. The parameters of the problem are a buoyancy ratio R quantifying the ratio of the relative contribution of B and A to the density as well as δ , the ratio of diffusion coefficients of these two species. We classify the region of RT, DD, DDD and DLC instabilities in the (R, δ) plane as a function of the elapsed time and show that, asymptotically, the unstable domain is much larger than the one captured on the basis of linear base-state profiles which can only obtain stability thresholds for the RT and DD instabilities. In addition the QSSA allows one to determine the critical time at which an initially stable stratification of A above B can become unstable with regard to a DDD or DLC mechanism when starting from initial step function profiles. Nonlinear dynamics are also analysed by a numerical integration of the full nonlinear model in order to understand the influence of R and δ on the dynamics.

Key words: buoyancy-driven instability, convection in porous media, double diffusive convection

1. Introduction

In porous media, a stratification of a given solution on top of another miscible solution is frequently encountered in applications related to soil contamination or

† Email address for correspondence: adewit@ulb.ac.be

chemical engineering for instance. Understanding the influence of possible buoyancy-driven instabilities of the interface between the two solutions is of interest in predicting mass transport properties. In this regard, it is well known that a Rayleigh–Taylor (RT) mechanism destabilizes the interface if a denser solution is put on top of a less dense one in the gravity field (Fernandez *et al.* 2002; Martin, Rakotomalala & Salin 2002). The interface then deforms into fingers that develop similarly above and below the interface (Wooding 1969; Manickam & Homsy 1995; Fernandez *et al.* 2002).

If the upper solution is less dense than the lower one, a double diffusive (DD) instability develops if the lower component is diffusing faster than the upper one. In the field of oceanography, such a DD instability has been studied in numerous works (Stommel, Arons & Blanchard 1956; Stern 1960; Turner 1979). Indeed, in the case of warm salty water overlying cold fresh water such that the overall density gradient is stable, so-called salt fingers are found to occur due to the diffusion of heat being greater than the diffusion of the salt. The literature on the salt fingering instability is vast and so the reader is referred to recent reviews for more details (Kunze 2003; Schmitt 2003). DD instabilities occur not only in mass/heat problems but also whenever two different solutes are present (Turner 1979; Cooper, Glass & Tyler 1997; Pringle & Glass 2002; D’Heroncourt, Zebib & De Wit 2006; D’Heroncourt, De Wit & Zebib 2007; Pritchard 2009). Hence, the term ‘double diffusive instability’ is often used in a general sense to refer to hydrodynamic instability scenarios implying simultaneous transfer of heat and mass or more generally of two scalar quantities diffusing at different rates. In this study, and throughout the rest of this paper, DD refers to the specific case of a buoyancy-driven instability triggered when a statically stable density gradient implies a competition between a less dense solution of a slower diffusing species overlies a denser solution of a faster diffusing species.

Linear stability analysis (LSA) of RT and DD instabilities is classically performed in porous media on the basis of linear base-state profiles of concentrations and/or temperature. The work by Nield (1968) and Nield & Bejan (2006) provides stability boundaries for these instabilities in a parameter space spanned by the Rayleigh numbers of the fast and slow diffusing species. However, such linear profiles are not adequate for all situations. Typically, in recent experimental work on RT and DD instabilities studied in Hele-Shaw cells, the initial condition is a step function between two miscible solutions of different properties. Fernandez *et al.* (2002) have performed experimental analysis of an RT instability in Hele-Shaw cells starting from a step profile of a denser solution on top of a less dense one. For the DD instability, Cooper *et al.* (1997) carried out a series of isothermal experiments inside a Hele-Shaw cell using a sucrose solution on top of a denser salt solution with again a step-like initial condition. The system yields a DD instability since the salt on the bottom diffuses approximately three times faster than the sucrose. Further experiments analysing the DD instability have also recently been performed by Pringle & Glass (2002). In their system, there exists a region of the parameter space where the threshold for this type of instability depends on time, a situation which cannot be described by an LSA based on linear or step-like base-state profiles.

In parallel, another kind of instability for such two-layer miscible stratifications can be obtained when, starting from a given solution overlying a denser solution, the solute on top diffuses faster than the one on the bottom. Initially, the density stratification is stable; however, in the course of time, regions with a locally unstable density gradient can develop because of the differential diffusivity of the two different solutes. Explicitly, as the upper solute diffuses faster downwards than the lower solute diffuses upwards, a depletion zone is created above the interface and an accumulation

zone forms below it. These two zones feature a situation where, locally, a denser solution lies above a less dense one, triggering convection symmetrically positioned, respectively, above and below the initial contact line. This kind of instability is referred to more specifically as diffusive-layer convection (DLC) as it is indeed induced by a differential diffusion effect. We will use here the DLC denomination to avoid any confusion with the ‘salt finger’ DD equivalent arising when the lower solute diffuses faster. The DLC instability has been studied experimentally by Turner & Stommel (1964) using a statically stable salinity gradient, which was then heated from below. Such an instability occurs, for instance, in the spring at the polar regions when the ice begins to melt, leading to cool fresh water overlying warmer saltier water. Concerning the solutal DLC case, Stern & Turner (1969), Shirtcliffe (1973) and Turner & Chen (1974) have performed isothermal experiments using sucrose and salt in a tank where now the fast diffusing salt is placed on top of the system. A detailed review of this instability was given by Huppert & Turner (1981). The DLC instability was also experimentally examined inside a Hele-Shaw cell by Griffiths (1981) using a sucrose solution above a salt solution. The situation is initially stable and the system becomes unstable only later in time, as explained in Stamp *et al.* (1998). As said above, the instability is due to the formation of two localized regions where a more dense liquid lies above a less dense liquid with the resulting convection taking place both above and below the interface. In such cases, predictions of the onset time of the instability can be performed only by considering time-dependent base-state profiles.

Recent experiments on buoyancy-driven instabilities of a reactive interface between two miscible solutions, with each containing a different reactant inside a Hele-Shaw cell (Zalts *et al.* 2008; Almarcha *et al.* 2010*a,b*), have renewed interest in understanding the onset conditions for the RT, DD and DLC instabilities. To be able to predict which instability is observed in these reactive systems when the initial condition is a step profile, it is crucial to understand how the underlying density profile evolves in time. As the base-state profiles are then time-dependent, the stability of the problem also depends on time and the classical LSA based on constant linear profiles is no longer valid. Before even tackling the reactive problem, the various instability scenarios first need to be analysed in detail for non-reactive miscible solutions.

In this context, the goal of this paper is to revisit the problem of buoyancy-driven instabilities of a miscible interface in a porous medium or a Hele-Shaw cell in the case where the initial density profile is a step function. Our objective is to classify the regions in the parameter space where the various RT, DD and DLC instability mechanisms are at play when a solution containing a species A overlies another miscible solution containing a different species B. Specifically, we take into account the time dependence of the base-state density profile when starting from a step function to predict at what time an instability is expected to occur and what its properties will then be. We identify an additional source of instability, which here refers to a delayed-double diffusive (DDD) instability occurring when the system is stable at $t = 0$ but is destabilized in time because solute B in the lower denser solution diffuses faster than solute A in the upper less dense solution. We classify the instability regions in a parameter space spanned by only two physical parameters, a buoyancy ratio R , measuring the relative contribution of each species to the density, and δ , the ratio of the diffusion coefficients. Before an instability occurs, convection is absent and so analytical diffusion solutions for the concentrations can be employed. We find that the corresponding one-dimensional (1-D) base-state density profiles can be classified into six different types and we identify in each case the possible instability mechanism. The onset time for destabilization is computed from an LSA using

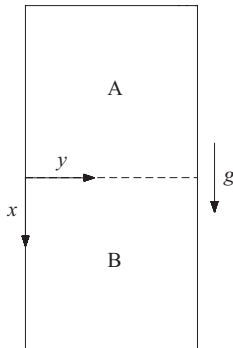


FIGURE 1. Sketch of the initial physical problem.

a quasi-steady-state approximation (QSSA), which also provides the instantaneous growth rate and wavenumber of the instability. The evolution of the corresponding nonlinear dynamical regimes is obtained using nonlinear simulations.

This paper is organized as follows. In § 2 the governing equations are presented and various types of base-state density profiles are described in the absence of convection. In § 3 the stability of the system is examined analytically using step functions, whilst in § 4 the stability of the time evolving profiles is examined numerically. In § 5 nonlinear simulations are presented to confirm the linear stability predictions as well as to predict the evolution of the system beyond the validity of the linear stability. The conclusions are drawn in § 6.

2. Model

Two different miscible solutions are placed in contact inside a vertically orientated 2-D porous medium or a Hele-Shaw cell in a configuration such as that sketched in figure 1. The upper solution contains a solute A in concentration A_0 whilst the lower solution contains a solute B in concentration B_0 . For simplicity, the domain size is assumed to be infinite. We define the y -axis as the horizontal axis and the x -axis as the vertical one which increases in the downwards direction, such that, as seen in figure 1, $x < 0$ is the upper region and $x > 0$ is the lower region.

The solutions are considered sufficiently dilute that the diffusion coefficients D_A and D_B of species A and B, respectively, can be considered as constant and the density ρ varies linearly with the concentrations in the form

$$\rho(A, B) = \rho_0[1 + \alpha_A A + \alpha_B B], \quad (2.1)$$

where A and B denote the concentration of their respective species, ρ_0 is the density of the pure solvent and the solutal expansion coefficients are defined as

$$\alpha_A = \frac{1}{\rho_0} \frac{\partial \rho}{\partial A} \quad \text{and} \quad \alpha_B = \frac{1}{\rho_0} \frac{\partial \rho}{\partial B}. \quad (2.2)$$

Both these parameters are taken positive since each solute is assumed here to increase the density. The Boussinesq approximation is made so that the flow can be treated as incompressible. Both liquids are assumed to have the same constant viscosity μ .

For a porous medium, the velocity evolution equation follows Darcy's law in which the buoyancy term depends on concentrations as in (2.1). For systems of constant porosity ϕ (Nield & Bejan 2006), the dimensional equations that describe the evolution

of this system are

$$\nabla p = -\frac{\mu}{K}\mathbf{u} + \rho(A, B)\mathbf{g}, \quad (2.3a)$$

$$\nabla \cdot \mathbf{u} = 0, \quad (2.3b)$$

$$\phi A_t + \mathbf{u} \cdot \nabla A = \phi D_A \nabla^2 A, \quad (2.3c)$$

$$\phi B_t + \mathbf{u} \cdot \nabla B = \phi D_B \nabla^2 B, \quad (2.3d)$$

where \mathbf{g} is the gravitational acceleration, p is the pressure field, subscript t denotes differentiation with respect to time and \mathbf{u} is the velocity vector. In the case of a vertically orientated Hele-Shaw cell, $\phi = 1$ and a sufficiently narrow gap width a is assumed so that Darcy's law is valid and the permeability $K = a^2/12$. Introducing $\Delta\rho = \alpha_A A_0$, a characteristic speed is given by the order of the buoyancy forces, namely

$$u_* = \frac{gK}{\nu} \Delta\rho, \quad (2.4)$$

where $\nu = \mu/\rho_0$ is the kinematic viscosity and g is the magnitude of the acceleration due to gravity. This allows one to construct the characteristic length $l_* = D_A \phi / u_*$ and time $t_* = l_*^2 / D_A$.

The equations in (2.3) are then non-dimensionalized using

$$t = t_* \hat{t}, \quad \mathbf{x} = l_* \hat{\mathbf{x}}, \quad \mathbf{u} = u_* \hat{\mathbf{u}}, \quad p = p_a + \rho_0 g l_* \hat{x} + \frac{\mu \phi D_A}{K} \hat{p}, \quad A = A_0 \hat{A}, \quad B = B_0 \hat{B}, \quad (2.5)$$

with p_a denoting the ambient pressure at $x = 0$ and where hats denote dimensionless variables. The density is non-dimensionalized as $\hat{\rho} = (\rho/\rho_0 - 1)/\Delta\rho$. Dropping hats for convenience, the resulting dimensionless equations describing the dynamics of the miscible two-layer system are the following:

$$\nabla p = -\mathbf{u} + (A + RB)\mathbf{i}_x, \quad (2.6a)$$

$$\nabla \cdot \mathbf{u} = 0, \quad (2.6b)$$

$$A_t + \mathbf{u} \cdot \nabla A = \nabla^2 A, \quad (2.6c)$$

$$B_t + \mathbf{u} \cdot \nabla B = \delta \nabla^2 B, \quad (2.6d)$$

where \mathbf{i}_x is the unit vector parallel to the x -axis and pointing downwards, while the ratio δ of the diffusion coefficients and the buoyancy ratio R are defined as

$$\delta = \frac{D_B}{D_A} \quad \text{and} \quad R = \frac{\alpha_B B_0}{\alpha_A A_0}. \quad (2.7)$$

The problem is closed through the initial conditions

$$A = 1, \quad B = 0, \quad \mathbf{u} = \mathbf{0} \quad \text{for } x < 0, \quad (2.8a)$$

$$A = 0, \quad B = 1, \quad \mathbf{u} = \mathbf{0} \quad \text{for } x > 0. \quad (2.8b)$$

2.1. Base state of the system

Before the onset of an instability, we can assume that the concentrations do not vary in the y direction and that the flow is at rest. Contrary to the classical stability analysis that uses fixed linear concentration profiles (Nield & Bejan 2006), the base state of our problem follows a diffusive dynamics, which satisfies (2.6c) and (2.6d) with $\mathbf{u} = \mathbf{0}$ along with the initial condition (2.8). The corresponding base-state solutions $\bar{A}(x, t)$

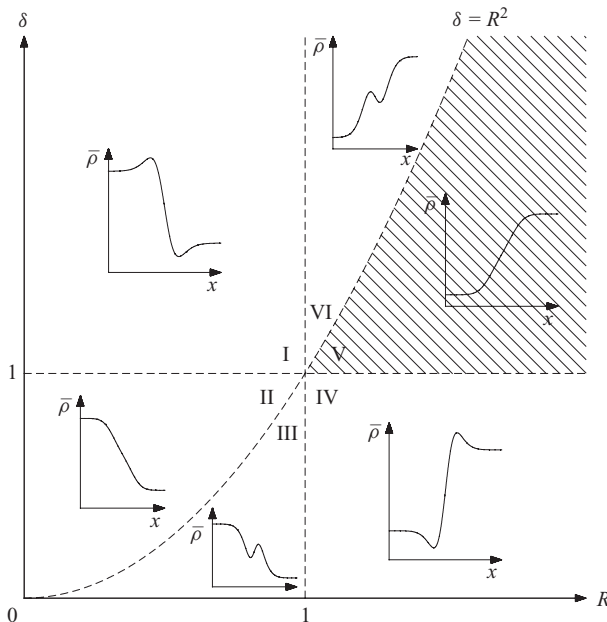


FIGURE 2. The six base-state density profile regions of the (R, δ) parameter space. Typical illustrations of $\bar{\rho}(x, t)$ are included within the corresponding regions. The shaded region corresponds to base-state density profiles, which are monotonic increasing.

and $\bar{B}(x, t)$ evolve analytically as

$$\bar{A} = \frac{1}{2} \operatorname{erfc}\left(\frac{x}{2\sqrt{t}}\right), \quad \bar{B} = \frac{1}{2} \operatorname{erfc}\left(-\frac{x}{2\sqrt{\delta t}}\right). \quad (2.9)$$

As an aide to the prediction of an instability, we first derive the base-state density profiles, illustrated in figure 2, which are constructed as

$$\bar{\rho}(x, t) = \bar{A}(x, t) + R\bar{B}(x, t). \quad (2.10)$$

At time $t=0$, we have, for $x < 0$, a uniform solution, where $(A, B) = (1, 0)$ of density $\bar{\rho} = 1$ overlying a uniform solution where $(A, B) = (0, 1)$ of density $\bar{\rho} = R$ at $x > 0$. The condition $R=1$ corresponds to the case where both solutes have the same density. For $R < 1$, we have a ‘heavy on top of light’ configuration, which is naturally unstable with regard to an RT instability. For $R > 1$, the system is initially in a stratifically stable ‘light on top of heavy’ configuration. Instabilities at $t=0$ can, however, occur if the two solutes diffuse at different rates. In particular, a DD instability is at play in some regions of the half-plane $\delta > 1$. In the zones of the (R, δ) plane stable at $t=0$ for $R > 1$, DLC can also occur later in the course of time if $\delta < 1$, due to the different rates of diffusion. This occurs when local regions in which a more dense fluid overlies a less dense fluid develop in time to yield an instability.

We notice that $\bar{\rho}(x, t) + \bar{\rho}(-x, t) = 1 + R$, so that the density is antisymmetric about $x=0$. More information on the spatial dependence of the density profile is obtained by analysing the gradient of the base-state density which is given by

$$\bar{\rho}_x = \frac{1}{2\sqrt{\pi t}} \left(\frac{R}{\sqrt{\delta}} \exp\left[-\frac{x^2}{4\delta t}\right] - \exp\left[-\frac{x^2}{4t}\right] \right). \quad (2.11)$$

The gradient $\bar{\rho}_x$ changes sign at the two points satisfying

$$x^2 = \frac{4t\delta}{1-\delta} \ln \left(\frac{R}{\sqrt{\delta}} \right), \quad (2.12)$$

when $(\delta - 1)(\delta - R^2) > 0$. A more complicated version of this condition for the case of cross-diffusion was given by Sasaki (1996).

Further, at $x=0$, the gradient is given by

$$\bar{\rho}_x|_{x=0} = \frac{1}{2\sqrt{\pi t}} \left(\frac{R}{\sqrt{\delta}} - 1 \right), \quad (2.13)$$

showing that the density gradient at $x = 0$ is locally positive for $R > \sqrt{\delta}$ and negative otherwise. Thus, a stable density profile monotonically increasing downwards occurs when

$$1 \leq \delta \leq R^2, \quad (2.14)$$

which is the shaded region in figure 2, whilst the five remaining unshaded regions have profiles in which a more dense fluid is above a less dense fluid either globally or at least in some region of space which can lead to an instability given a sufficient amount of time.

Thus, the (R, δ) parameter space can be divided into six regions depending on the general trend of the base-state density profiles, as illustrated in figure 2. The RT domain $0 < R < 1$ is divided into three regions corresponding to the three types of possible density profiles, each of which are stratifically unstable as they feature a denser solution of A on top of a less dense solution of B. The top left region I, for $\delta > 1$, has density profiles which contain two local extrema which move in time in opposite directions away from the interface. The middle left region II, for $1 > \delta > R^2$, has monotonic decreasing density profiles. The bottom left region III, for $1 > R^2 > \delta$, has density profiles containing a local stratifically stable region near the interface, surrounded by two stratifically unstable regions.

The domain $R > 1$ is also divided into three regions, each of which is initially stratifically stable with less dense A on top of denser B. Instabilities can thus result only from differential diffusive processes. The top right region VI, for $\delta > R^2 > 1$, has density profiles which evolve to yield a locally stratifically unstable region around the interface. The middle right region V, for $R^2 > \delta > 1$, has stable monotonic increasing density profiles and the bottom right region IV, for $\delta < 1 < R$ has density profiles which contain two local extrema which move away from the interface in time, leading to two locally stratifically unstable regions.

Although the base-state density profiles provide a strong insight into any anticipated instability, the actual conditions and the time for an instability to occur are determined using an LSA of a time evolving base state.

3. Linear stability analysis

As the flow is incompressible, for convenience, the stream function ψ formulation is employed. Using $u = \psi_y$ and $v = -\psi_x$, where $\mathbf{u} = (u, v)$, we satisfy $\nabla \cdot \mathbf{u} = 0$. Taking the curl of (2.6a) and substituting ψ into (2.6c) and (2.6d) yields the following system of equations

$$\nabla^2 \psi = A_y + RB_y, \quad (3.1a)$$

$$A_t + \psi_y A_x - \psi_x A_y = \nabla^2 A, \quad (3.1b)$$

$$B_t + \psi_y B_x - \psi_x B_y = \delta \nabla^2 B. \quad (3.1c)$$

We introduce normal form perturbations to the base-state solutions in the form

$$[\psi, A, B] = [0, \bar{A}, \bar{B}] + \epsilon e^{\sigma t + ik y} [ik^{-1} \mathcal{F}, \mathcal{A}, \mathcal{B}], \quad (3.2)$$

where ϵ is a small parameter and we have made the QSSA by assuming that the base state is varying more slowly than the perturbations. We now consider the base-state solution at a given time t_0 . Linearizing system (3.1) in ϵ , we obtain

$$\mathcal{F}_{xx} = k^2(\mathcal{F} + \mathcal{A} + R\mathcal{B}), \quad (3.3a)$$

$$\sigma \mathcal{A} = \mathcal{A}_{xx} - k^2 \mathcal{A} + \bar{A}_x \mathcal{F}, \quad (3.3b)$$

$$\sigma \mathcal{B} = \delta(\mathcal{B}_{xx} - k^2 \mathcal{B}) + \bar{B}_x \mathcal{F}. \quad (3.3c)$$

Although we have analytical solutions for \bar{A}_x and \bar{B}_x , numerics are employed to obtain the growth rate σ of the instability as a function of its wavenumber k to determine the dispersion curves.

3.1. Stability of the system at $t_0 = 0$

At time $t_0 = 0$, the base-state concentration profiles are step functions; hence, $\bar{A}_x = \bar{B}_x = 0$ for $x \neq 0$ and an analytical expression of the dispersion curves can be obtained following the approach of Tan & Homsy (1986). For $x \neq 0$, the bulk linear stability equations become

$$g_1^2 \mathcal{A} = \mathcal{A}_{xx}, \quad g_2^2 \mathcal{B} = \mathcal{B}_{xx}, \quad \mathcal{F}_{xx} = k^2(\mathcal{F} + \mathcal{A} + R\mathcal{B}), \quad (3.4)$$

where $g_1^2 = k^2 + \sigma$ and $g_2^2 = k^2 + (\sigma/\delta)$. Using the conditions \mathcal{A}, \mathcal{B} and $\mathcal{F} \rightarrow 0$ as $x \rightarrow \pm\infty$ and the fact that \mathcal{A}, \mathcal{B} and \mathcal{F} are continuous at $x = 0$ yield

$$\mathcal{A} = \alpha e^{-g_1|x|}, \quad \mathcal{B} = \beta e^{-g_2|x|}, \quad \mathcal{F} = \frac{\alpha}{\sigma} k^2 e^{-g_1|x|} + \frac{\beta}{\sigma} R \delta k^2 e^{-g_2|x|} + \gamma e^{-k|x|}, \quad (3.5)$$

where α, β and γ are the amplitudes of these eigenfunctions. Integrating (3.3a) from $x = -\epsilon$ to $x = \epsilon$ and letting ϵ tend to zero imply that \mathcal{F}_x is continuous at $x = 0$ and thus

$$\gamma = -\alpha \frac{g_1 k}{\sigma} - \beta \frac{g_2 k}{\sigma} R \delta, \quad (3.6)$$

which ensures that the velocities, and hence the derivatives of ψ , are continuous at $x = 0$. Although the initial base-step profiles are discontinuous, the functions \bar{A}_x and \bar{B}_x can be treated as delta functions at $t_0 = 0$, since they are zero for $x \neq 0$ but they satisfy $\int_{-\infty}^{\infty} \bar{A}_x dx = -1$ and $\int_{-\infty}^{\infty} \bar{B}_x dx = 1$. Hence, integrating (3.3b) and (3.3c) from $x = -\epsilon$ to $x = \epsilon$, using

$$\int_{-\epsilon}^{\epsilon} \bar{A}_x \mathcal{F} dx = -\mathcal{F}(0), \quad \int_{-\epsilon}^{\epsilon} \bar{B}_x \mathcal{F} dx = \mathcal{F}(0), \quad (3.7)$$

and letting $\epsilon \rightarrow 0$ lead to $[\mathcal{A}_x]_{-\epsilon}^{\epsilon} = -\delta[\mathcal{B}_x]_{-\epsilon}^{\epsilon} = \mathcal{F}(0)$, which yield the conditions

$$-2\sigma g_1 \alpha = 2\sigma \delta g_2 \beta = k[\alpha(k - g_1) + R\delta\beta(k - g_2)]. \quad (3.8)$$

Hence, $\beta = -g_1 \alpha / (\delta g_2)$ and the dispersion relation is obtained as

$$1 - \frac{k}{g_1} = R \left(1 - \frac{k}{g_2} \right) + \frac{2\sigma}{k}, \quad (3.9)$$

which is identically equal to

$$1 - \frac{k}{\sqrt{k^2 + \sigma}} = R \left(1 - \frac{k}{\sqrt{k^2 + (\sigma/\delta)}} \right) + \frac{2\sigma}{k}. \quad (3.10)$$

Further, the eigenfunction associated with the stream function can be obtained and normalized using $\alpha = -1/(2g_1)$, so that $\mathcal{F}(0) = 1$, to yield

$$\mathcal{F} = \frac{k}{2\sigma} \left[(1-R)e^{-k|x|} - \frac{k}{g_1} e^{-g_1|x|} + \frac{kR}{g_2} e^{-g_2|x|} \right]. \quad (3.11)$$

We notice that $\mathcal{F}_x = 0$ at $x=0$. This means that, at $t_0=0$, the LSA predicts that even when the system is unstable, the disturbance to the horizontal velocity v will be zero at the initial interface so that only perturbations to the vertical velocity will grow in time at the initial interface.

3.2. Limiting cases at $t_0=0$

The instantaneous growth rates are implicitly defined by (3.10). However, one can explicitly obtain these growth rates for a small number of degenerate cases.

The case $R=0$, or equivalently $\delta \rightarrow \infty$, in (3.10) yields

$$\sigma = \frac{k}{2}(1-k-\sqrt{k(k+2)}), \quad (3.12)$$

which corresponds to the pure RT instability of a layer of A above the pure solvent where $B_0=0$, which is always unstable (see Manickam & Homsy 1995 and De Wit 2001). Such a situation has been studied experimentally in Hele-Shaw cells by Fernandez *et al.* (2002) for instance. The maximum growth rate $\sigma_{max} = (5\sqrt{5} - 11)/8$ occurs at $k_{max} = (\sqrt{5} - 2)/2$ and the cut-off wavenumber $k_{cut} = 1/4$.

If $\delta = 1$, no differential diffusion effects are possible and the only possible instability is an RT one when $R < 1$, i.e. when a denser solution of A overlies a less dense solution of B. Setting $\delta = 1$ in (3.10) yields

$$\sigma = \frac{k}{2}(1-R-k-\sqrt{k[k+2(1-R)]}), \quad (3.13)$$

which indeed requires $R < 1$ for an instability to occur. The maximum growth rate $\sigma_{max} = (1-R)^2(5\sqrt{5} - 11)/8$ occurs at $k_{max} = (1-R)(\sqrt{5} - 2)/2$; with a cut-off wavenumber, $k_{cut} = (1-R)/4$.

The case $\delta=0$ physically corresponds to an immobile species B; however, it also provides a good approximation to the case when A diffuses much faster than B. In the limit $\delta \rightarrow 0$ in (3.10), by writing $p = 1 - R$, the real growth rate is given by

$$\sigma = \frac{k}{3} \left(p - k - (p + 2k) \cos \left[\frac{\pi}{3} + \frac{2}{3} \cos^{-1} \sqrt{\frac{27k}{2(p+2k)^3}} \right] \right), \quad (3.14)$$

for $k \leq (3 \cos[(\pi + \cos^{-1} p)/3] - p)/2$, which has a corresponding maximum growing wavenumber given by $k_{max} = (4/\sqrt{6}) \cos[(\pi + \cos^{-1}(p\sqrt{27/32}))/3] - (p/2)$. However, the maximum growth rate is real only when R is less than 0.37027 and it is complex for R greater than this value, so that oscillatory instabilities may initially be present.

3.3. Instantaneous growth rates at $t_0=0$

For other pairs of parameters (R, δ) , (3.10) is solved numerically to determine σ for a given k . When $\delta > 1$, i.e. when the solute in the lower layer diffuses fastest, one finds that the instantaneous growth rates are always real. Typical dispersion curves are plotted when $\delta=3$ for various values of R in figure 3(a). The most unstable case is obtained for $R=0$, i.e. a dense A on top of a buoyantly neutral B (diffusing faster). As R increases, both the maximum value of the instantaneous growth rate and the maximum growing wavenumber decrease because the density difference

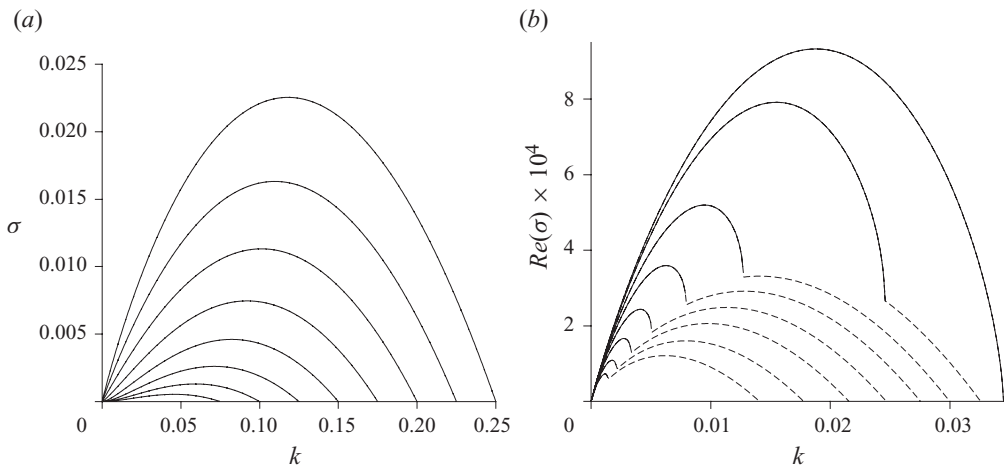


FIGURE 3. Instantaneous growth rates against k at $t_0=0$ for (a) $\delta=3$ and various R ranging from $R=0$ at the top to $R=2.1$ at the bottom in uniform increments of 0.3 ; (b) $R=0.75$; the results are illustrated for $\delta=0.87, 0.82, 0.68, 0.55, 0.4, 0.25, 0.1$ and 0.01 from top to bottom. Solid curves indicate real growth rates and dashed curves indicate complex growth rates.

between the upper solution of A and the lower solution of B decreases. As long as $R < 1$, the system remains RT-unstable. Once $R > 1$, the system is RT-stable; yet DD instabilities take over as $\delta > 1$. It is observed that the decrease of the dispersion curve is monotonous when R switches from the RT-unstable regime ($R < 1$) to the DD unstable one ($\delta > R > 1$). When $\delta \geq 1$, the eigenfunction associated with the stream function is found to take its maximum value at the initial interface at $x=0$, i.e. both RT and DD instabilities develop at the interface. When $\delta < 1$, the instantaneous growth rate σ can become complex (figure 3b), which generalizes the analytical result found when $\delta=0$. These complex σ appear below the line $\delta = R^2$ with $\delta < 1$. This is the same condition illustrated in figure 2 for the base-state density profile to exhibit a stratifically stable zone sandwiched between two stratifically unstable zones when $t > 0$. Typical dispersion curves are plotted for $R=0.75$ and various values of δ in figure 3(b). As δ decreases, the maximum value of σ also decreases; however, the maximum growing wavenumber is not monotonic decreasing due to a switch from a real mode to the complex mode which occurs at a larger wavenumber.

3.4. Neutral stability curves at $t_0=0$

The neutral stability lines can be determined analytically for arbitrary values of δ and R . To determine the maximum growing wavenumber, one needs to consider $\text{Re}(d\sigma/dk)=0$, which yields

$$0 = \text{Re} \left(\sigma - \frac{2\sigma}{4 + Rk^2\delta^{-1}(k^2 + \sigma/\delta)^{-3/2} - k^2(k^2 + \sigma)^{-3/2}} \right). \quad (3.15)$$

For $\delta > 1$, with $0 < \delta - R \ll 1$ and $\delta - R \ll \delta - 1$, we can expand (3.10) and (3.15) to yield

$$k_{max} = \frac{\delta - R}{6\delta} - \frac{5(\delta + 1)(\delta - R)^2}{3^5\delta^2(\delta - 1)} + \mathcal{O}((\delta - R)^3), \quad (3.16)$$

$$\sigma_{max} = \frac{(\delta - R)^3}{3^4\delta^2(\delta - 1)} + \frac{(10\delta - 17)}{3^7\delta^3(\delta - 1)^2}(\delta - R)^4 + \mathcal{O}((\delta - R)^5). \quad (3.17)$$

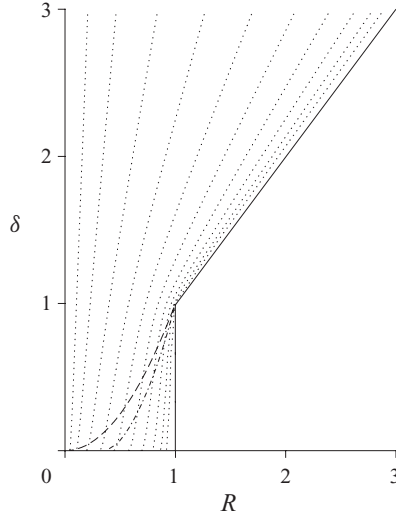


FIGURE 4. Contours of the maximum real part of the growth rate, $[\text{Re}(\sigma)]_{\max}$ in the (R, δ) parameter space at $t_0 = 0$. The solid lines correspond to $[\text{Re}(\sigma)]_{\max} = 0$. The dashed curve is the line $\delta = R^2$ for $R < 1$ and the dot-dashed curve below it separates the oscillatory region below it from the region with real growth rates above it. The dotted contours correspond to $[\text{Re}(\sigma)]_{\max} = 0.02 \exp(-0.1n^2)$ for $n = 1$ to 10 from left to right.

Thus, both k_{\max} and σ_{\max} approach zero as δ approaches R . The cut-off wavenumber is $k_{\text{cut}} = (\delta - R)/(4\delta)$ for $\delta > R > 1$. For $\delta < 1$ with $0 < 1 - R \ll 1$ and $1 - R \ll (1 - \sqrt{\delta})$ by expanding (3.10) and (3.15), we find that the most unstable mode is the complex root given by

$$k_{\max} = (2 + \sqrt{2}) \left(\frac{(1 - R)^3}{8(1 - \sqrt{\delta})^2} - \frac{\sqrt{\delta}(1 - R)^4}{4(1 - \sqrt{\delta})^3} + \mathcal{O}((1 - R)^5) \right), \quad (3.18)$$

$$\sigma_{\max} = (1 - i\sqrt{11 + 8\sqrt{2}}) \left(\frac{(1 - R)^4}{32(1 - \sqrt{\delta})^2} - \frac{\sqrt{\delta}(1 - R)^5}{16(1 - \sqrt{\delta})^3} + \mathcal{O}((1 - R)^6) \right). \quad (3.19)$$

Thus, both k_{\max} and σ_{\max} approach zero as R approaches 1. Hence, as shown in figure 4, the neutral stability lines are $\delta = R$ for $\delta > 1$ and $R = 1$ for $\delta < 1$.

Numerically solving (3.10) allows us to obtain the maximum real part of the growth rate. In figure 4, contours of $[\text{Re}(\sigma)]_{\max}$ are illustrated in the (R, δ) plane. It is seen that increasing R at fixed δ or reducing δ at fixed $R < \max(1, \delta)$ lead to a decrease in the maximum real part of the growth rate.

The LSA using step functions for the concentrations mean that, for initially separated species, the DD instability has an onset condition $\delta > R$ when $\delta > 1$ (a denser solute diffusing faster than the overlying less dense solute).

To summarize, figure 4 shows that if $R < 1$, the system is always unstable with respect to RT. If $R > 1$, then DD occurs at $t_0 = 0$ for an initial step function condition when $\delta > R$. The rest of the (R, δ) plane, i.e. the zone where $R > 1$ and $\delta < R$, is stable at $t_0 = 0$, which is smaller than the stable region when linear base-state profiles are used. As we will show next, some parts of the stable region in figure 4 can, however, be destabilized in time.

4. Linear stability analysis for evolving profiles

In the previous section, the analytical dispersion equation (3.10) was obtained for the initial condition when the concentration fields are step functions. In this case, the neutral stability curve at $t_0 = 0$ can be obtained analytically. At $t > 0$, as the base-state concentration profiles evolve in time, the stability of the system also changes in time. The instability conditions have then to be determined numerically. To do so, the infinite domain is truncated to a finite size L_x . We discretize (3.3a)–(3.3c) using a finite-difference scheme (Kalliadasis, Yang & De Wit 2004) to yield

$$\mathbf{L}\mathcal{F} = k^2(\mathcal{A} + R\mathcal{B}), \quad (4.1a)$$

$$\sigma\mathcal{A} = \mathbf{D}_x^{(a)}\mathcal{F} + \mathbf{L}\mathcal{A}, \quad (4.1b)$$

$$\sigma\mathcal{B} = \mathbf{D}_x^{(b)}\mathcal{F} + \delta\mathbf{L}\mathcal{B}, \quad (4.1c)$$

where the fields \mathcal{F} , \mathcal{A} and \mathcal{B} are now evaluated at discrete points and are represented in vector notation by \mathcal{F} , \mathcal{A} and \mathcal{B} . The diagonal matrices $\mathbf{D}_x^{(a)}$ and $\mathbf{D}_x^{(b)}$ are constructed from the base-state solutions with their diagonal elements defined as $D_{jj}^{(a)} = \bar{A}_{xj}$ and $D_{jj}^{(b)} = \bar{B}_{xj}$. The linear operator $(\partial_x^2 - k^2)$ is expressed in matrix format using finite differences as \mathbf{L} . By expressing the eigenvector \mathcal{F} as

$$\mathcal{F} = k^2\mathbf{L}^{-1}\mathcal{A} + Rk^2\mathbf{L}^{-1}\mathcal{B}, \quad (4.2)$$

the eigenvalue problem reduces to

$$\sigma \begin{pmatrix} \mathcal{A} \\ \mathcal{B} \end{pmatrix} = \begin{pmatrix} \mathbf{L} + k^2\mathbf{D}_x^{(a)}\mathbf{L}^{-1} & Rk^2\mathbf{D}_x^{(a)}\mathbf{L}^{-1} \\ k^2\mathbf{D}_x^{(b)}\mathbf{L}^{-1} & \delta\mathbf{L} + Rk^2\mathbf{D}_x^{(b)}\mathbf{L}^{-1} \end{pmatrix} \begin{pmatrix} \mathcal{A} \\ \mathcal{B} \end{pmatrix}. \quad (4.3)$$

The matrix \mathbf{L}^{-1} was numerically obtained using the subroutine DGESV from LAPACK, and the eigenvalues and eigenvectors were obtained using DGEEVX from LAPACK. Thus, for a given wavenumber k , the growth rate σ can be obtained. As the base-state solution varies quickly at the start, this method is not valid for small values of t_0 .

As the wavenumber k tends to zero, the domain size L_x must tend to infinity. Numerically, it was found that setting $L_x = 16\pi/k$ was usually sufficiently large, but sometimes the domain required must be considerably larger than this. However, for moderate and large wavenumbers, this setting can lead to the domain size being too small to fully capture the diffusive length scale. Hence, we did not allow L_x to be less than $8\sqrt{(1+\delta)t_0}$. With the base states and, in some cases, the eigenfunctions evolving on different length scales, it was found more efficient to discretize this problem using a non-uniform grid. The vertical spatial coordinate x was defined on a discrete set of $N + 1$ points given by

$$x_j = j \frac{L_x}{N} \left(\frac{16}{L_x} \sqrt{t_0 + 1} \right)^{1-2|j/N|}, \quad (4.4)$$

with the integer $|j| \leq N/2$ so that $|x_j| \leq L_x/2$ and the mesh is finest around $x_0 = 0$ with $x_1 \approx 16\sqrt{t_0 + 1}/N$. This smallest spatial step was used to ensure that the variation of the base-state concentrations was adequately included. Grid independence was

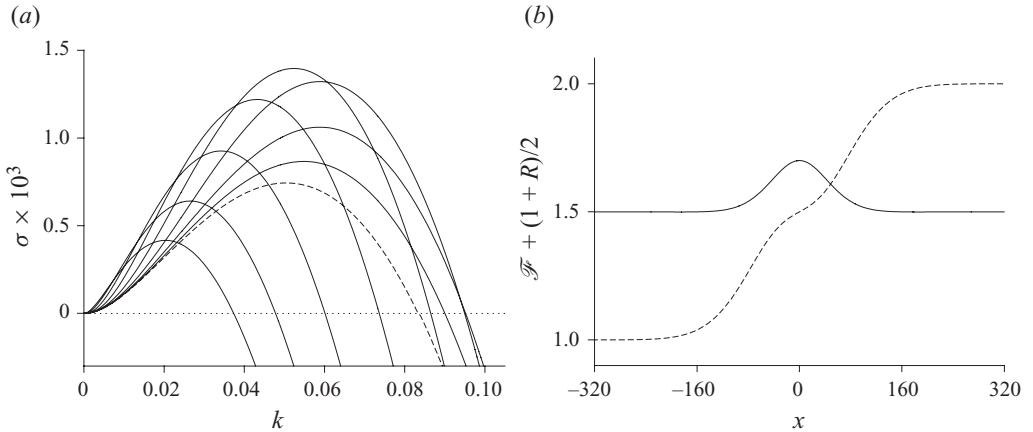


FIGURE 5. Characteristics of a DD instability for $\delta = 3$ and $R = 2$, i.e. $\delta > R > 1$. In (a) dispersion curves are illustrated at times $t_0 = 0$ (dashed curve) and $t_0 = 10^n$, where $n = 0.5-4$ in uniform increments of 0.5. In (b) the eigenfunction associated with the stream function is illustrated at $t_0 = 10^3$. The eigenfunction \mathcal{F} has been scaled to have an amplitude of $(R-1)/5$. The base-state density field is represented by a dashed line.

checked by increasing N until the variation in the maximum growth rate was below a given tolerance. Typically, $N = 200$ was found to provide sufficiently accurate results.

4.1. Double diffusive instability

An important case to examine is the DD instability that occurs when a given solution overlies a denser one with the solute on the bottom diffusing faster. This is the case when a sugar solution is placed above a denser salt solution for instance, as salt diffuses approximately three times faster. We have seen that, at $t_0 = 0$, DD occurs for $\delta > R > 1$. To appreciate the changes in stability in time, dispersion curves are illustrated in figure 5(a) at various times for a case already unstable at $t_0 = 0$, i.e. for $\delta > R > 1$. A dashed line is used to denote the dispersion curve at $t_0 = 0$ obtained analytically using (3.10), whilst the remaining dispersion curves at later times were obtained numerically. For these particular parameter values, the growth rate is real and the maximum growth rate initially increases in time; however, by $t_0 = 10^2$, it starts to decrease. Similarly, the maximum growing wavenumber initially increases in time and then starts to decrease around $t_0 = 10^{1.5}$.

4.2. Limit of validity of the QSSA

An inspection of figure 5(a) raises the following question: what is the limit of validity of the QSSA? If the system is already unstable at $t_0 = 0$, as in figure 5(a) (dashed curve), what is the meaning of the other dispersion curves computed at later times if the base state has already been perturbed by the instability and, in a sense, is replaced by convecting dynamics? To answer this question, it is important to realize that, at onset, the growth rate of the instability is very small. To understand at what time the perturbations have grown sufficiently so that the diffusive base state no longer exists, we plot the predicted maximum growth rate from the LSA, i.e. $[\text{Re}(\sigma)]_{\max}$, against time. In figure 6, this quantity is compared to the actual growth rate obtained from full nonlinear simulations by measuring the slope of the curve $d(\ln \gamma_k)/dt$ in the linear regime where γ_k is the amplitude of a spatial mode in the Fourier transform of the axially averaged signal. This quantity is plotted in figure 6

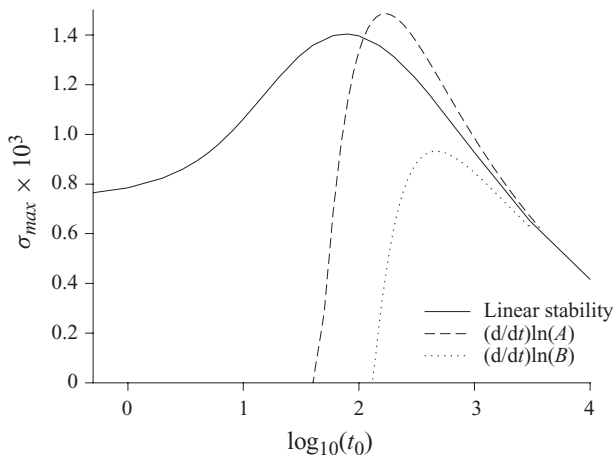


FIGURE 6. The maximum instantaneous growth rate σ_{max} is plotted against the logarithm of t_0 for $R=2$ and $\delta=3$. Both the predicted maximum growth rate obtained from the LSA and the actual growth rate obtained from full numerical simulations are given.

for both concentrations A and B . We note that the magnitude of the term $[\text{Re}(\sigma)]_{max} t_0$ is important in determining the order of the time at which the instability becomes physically observable. We find that once the term $[\text{Re}(\sigma)]_{max} t_0$ is of order one, the LSA predicts that this magnitude increases monotonically. So the amplitude of some perturbations will grow exponentially on a time scale $t_\sigma = [\text{Re}(\sigma)]_{max}^{-1}$. This is why after several t_σ , the base-state concentration fields become invalid, and hence, the LSA is also no longer valid. We conclude that the QSSA loses any meaning for $t_0 \gg t_\sigma$. As a consequence, we cannot trust the obtained dispersion curves far beyond the time t_σ , which, in figure 5(a), is $t_\sigma \sim 10^3$.

The dispersion curves in figure 5(a) allowed us to examine the evolution of the maximum growing wavenumber and growth rate in time. The region where the instability occurs can then be identified from the eigenfunction associated with the maximum growth rate. In figure 5(b), the eigenfunction associated with the stream function is illustrated at $t_0 = 10^3$, when $\sigma_{max} t_0$ is close to unity. The base-state density profile is included in figure 5(b) so that the location of the instability in the fluid flow can be correlated to the density profile. We observe that the instability is localized around the position where the two liquids initially came into contact, i.e. $x=0$.

4.3. A delayed-double diffusive instability

Let us next analyse a case when the system is initially stable, i.e. such that $R > \delta > 1$. In that case, all growth rates are negative at $t_0 = 0$ (see figure 4). However, as shown in figure 7(a), for $\delta = 3$ and $R = 4$, the growth rates can become positive in the course of time. Again the maximum growing wavenumber initially increases in time and then later decreases in time. To distinguish this type of instability, which arises only at later $t_0 > 0$, from the DD, which is readily unstable at $t_0 = 0$ and is shown in figure 5(a), we introduce the term DDD instability. This describes the situation when a ‘light over heavy’ density profile which is initially stable becomes unstable in time for $\delta > 1$, i.e. when the lower solute diffuses faster.

From figure 7(a), we find that $\sigma_{max} t_0$ is close to unity at $t_\sigma \sim 10^5$ for $\delta = 3$ and $R = 4$. In figure 7(b), the corresponding eigenfunctions associated with the stream function and base-state density profile are illustrated at $t_0 = 10^5$. We observe that, as for DD,

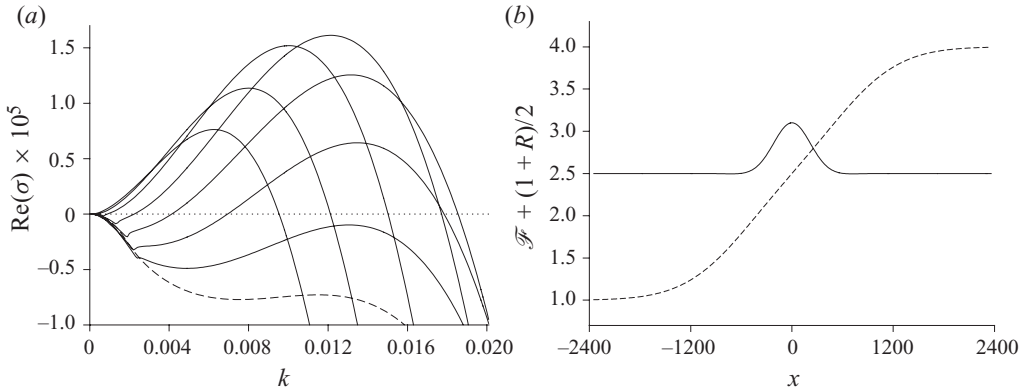


FIGURE 7. A DDD instability for $\delta=3$ and $R=4$. In (a) dispersion curves are illustrated at times $t_0 = 1500$ (dashed), 2000, 3000, 5000, $t_0 = 10^4, 10^{4.5}, 10^5$ and $10^{5.5}$; (b) eigenfunction associated with the stream function for $\delta=3$ with $R=4$ at $t_0 = 10^5$. The eigenfunction \mathcal{F} has been scaled to have an amplitude of $(R-1)/5$. The base-state density field is represented by a dashed line.

the DDD instability is localized around the position where the two liquids initially came into contact, i.e. $x=0$.

The time at which σt_0 becomes order 1 is important, as this represents the time at which the initial disturbances start to become large. The time at which the growth rates first become positive is also important since it represents the actual time of birth of the instability. Neutral stability curves, i.e. the loci of parameter values at the onset of the instability, are thus also functions of time. A large-time asymptotic limit was considered and, by approximating the error functions by linear profiles, it was found that the neutral stability curve for a DDD instability can be expressed in the form

$$\delta = R^{2/3} + \mathcal{O}(t_0^{-1/4}), \quad (4.5)$$

for a given onset time t_0 and further the onset wavenumber, $k \sim \mathcal{O}(t_0^{-3/8})$.

To test this theory, the critical value of δ for a given R and onset time t were calculated numerically. In figure 8(a), $\log(\delta_c - R^{2/3})$ is plotted against $\log(t_0)$ for $R=2$ and $R=4$, where δ_c is the value of δ for the onset of an instability at time t_0 . In figure 8(b), $\log(k)$ is plotted against $\log(t_0)$, where k and t_0 are the corresponding onset wavenumber and onset time.

The numerically obtained LSA results in figure 8 are in agreement with the predicted large-time asymptotic analysis, i.e. $\delta_c - R^{2/3} \sim t_0^{-1/4}$ and $k \sim t_0^{-3/8}$. In particular, one notices that as t_0 tends to infinity, the neutral stability curve approaches $R = \delta^{3/2}$, which is a well-known analytical result for this problem when the concentration fields are linear functions of the vertical direction. When $t_0 \rightarrow \infty$ our time-dependent stability analysis of concentration profiles evolves as (2.9) recovers, the classical result obtained using linear base states (Huppert & Manins 1973). For $\delta > 1$, the maximum growth rates were always found to be real.

4.4. Diffusive-layer-convection instability

Another important case to examine is the DLC instability that occurs when a given solution is placed above a denser solution ($R > 1$), but now the fastest diffusing solute is in the upper layer, i.e. $\delta < 1$. This corresponds to a salt solution on top of a denser sugar solution, for instance, for which $\delta=0.3$ typically. This instability occurs due to the formation of two locally stratificationally unstable regions (see figure 2, zone IV).

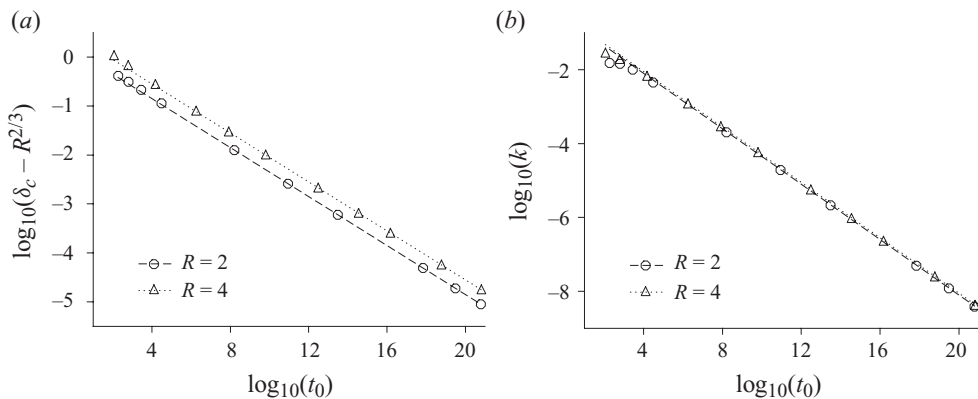


FIGURE 8. DDD instabilities. In (a) $\log(\delta_c - R^{2/3})$ is plotted against $\log(t_0)$, whilst in (b) $\log(k)$ is plotted against $\log(t_0)$. The markers represent data from the numerical LSA. In (a) the dashed line for $R=2$ is $\log(\delta - 2^{2/3}) = 0.15 - (1/4)\log(t_0)$ and the dotted line for $R=4$ is $\log(\delta - 4^{2/3}) = 0.45 - (1/4)\log(t_0)$. In (b) the dashed line for $R=2$ is $\log(k) = -0.6 - (3/8)\log(t_0)$ and the dotted line for $R=4$ is $\log(k) = -0.55 - (3/8)\log(t_0)$.

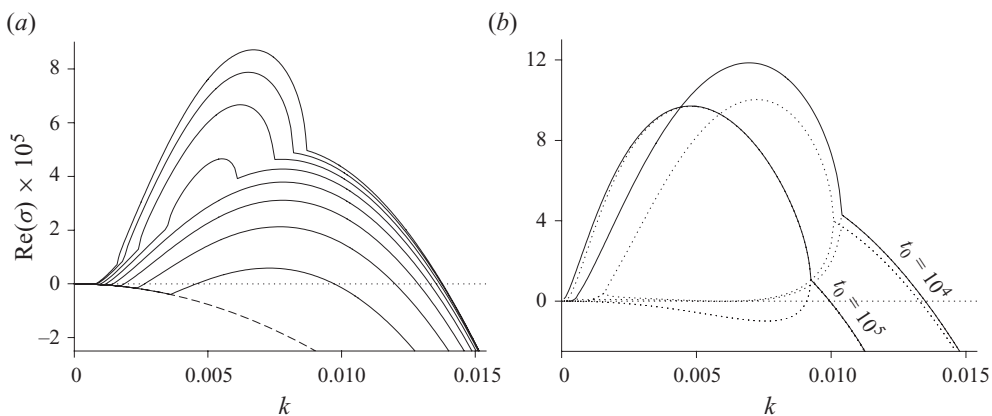


FIGURE 9. Dispersion curves at various times for $\delta=0.3$ and $R=1.1$ for a DLC instability. In (a) the growth rate with the maximum real part is illustrated for $t_0 = 10^3$ (dashed) to 5×10^3 in uniform increments of 5×10^2 from bottom to top, whilst in (b) the four growth rates whose real parts are largest are illustrated for $t_0 = 10^4$ and $t_0 = 10^5$. The solid curves represent the growth rate with the largest real part for a given t_0 while the dotted curves represent the next three growth rates with the largest real parts.

In the upper layer, a depletion of mass occurs due to the faster diffusion of the upper species downwards, whilst in the lower layer, an accumulation of mass results from the slower diffusion of the lower species upwards. Typical dispersion curves for this case are illustrated at various times in figure 9.

The DLC instability occurs in the $R > 1 > \delta$ region which is stable at $t_0 = 0$ (see figure 4). Eventually, after a certain amount of time, depending on R and δ , the system becomes unstable with a complex growth rate. For the particular case illustrated in figure 9(a), the instability onset time is a little before $t_0 = 1.5 \times 10^3$. Although the maximum growth rate of the system remains complex for a certain period of time, eventually the maximum growth rate becomes real. The maximum growing wavenumber associated with the real growth rate is smaller than the one associated

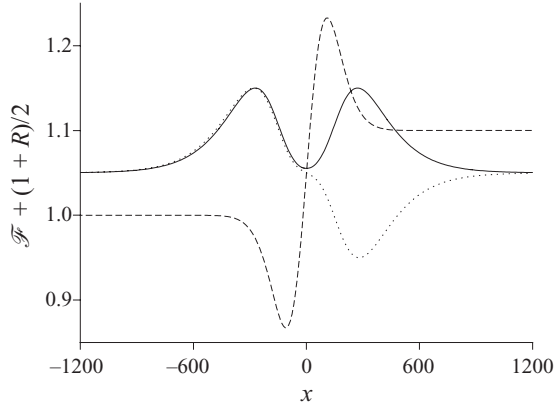


FIGURE 10. The eigenfunctions associated with the stream function for $\delta=0.3$ and $R=1.1$ at $t_0=10^4$ for a DLC instability with σt_0 close to unity. The eigenfunction associated with the maximum growth rate of the first and second branches are the solid and dotted lines, respectively. The eigenfunctions \mathcal{F} have been scaled to have an amplitude of 0.1. The base-state density field is represented by a dashed line.

with the complex growth rate at a given time. Numerically, one finds that the product of the time taken for the growth rate to become real and the maximum growth rate is much less than unity, and thus the system is still in the early stages of the linear regime, i.e. the system has not entered the nonlinear regime and so one would not expect the early complex growth rates to result in any oscillatory behaviour. For the particular case illustrated in figure 9(a), the maximum growth rate becomes real around $t_0 = 5.5 \times 10^3$.

For a certain period of time, both the maximum growing wavenumber, associated with the real growth rate, and the growth rate increase in time, but as time increases, eventually the growth rate and wavenumber start to decrease. This can be explained as follows. The system is initially stable as diffusion has not yet taken place. As time increases, the diffusive process leads to the formation of two locally stratifically unstable regions. The system remains stable for a certain period of time until, eventually, the stratifically unstable regions build up a sufficiently large amount of mass to trigger a destabilization. However, for sufficiently larger times, this mass is distributed over an ever larger region and the density gradients become ever smaller, and so the system becomes less unstable in time.

In the large-time regime, one finds that it is vital to consider the additional modes that are present, as shown in figure 9(b). Such a behaviour is important as it means that any resulting instability will involve two different eigenfunctions. In order to gain insight into the behaviour of the fluid flow, it is useful to examine the eigenfunction associated with the stream function of the most unstable mode. At large times, the eigenfunction associated with the stream function of the most unstable mode is symmetric about $x=0$ whilst the second most unstable mode is an eigenfunction antisymmetric about $x=0$, as shown in figure 10. This implies that the instabilities in the upper and lower regions will become independent of each other.

Some preliminary results for the DLC instability have already been obtained in experiments; however, using non-steady concentration profiles has allowed the LSA to predict this DLC instability region, which was missed by the LSA using linear profiles.

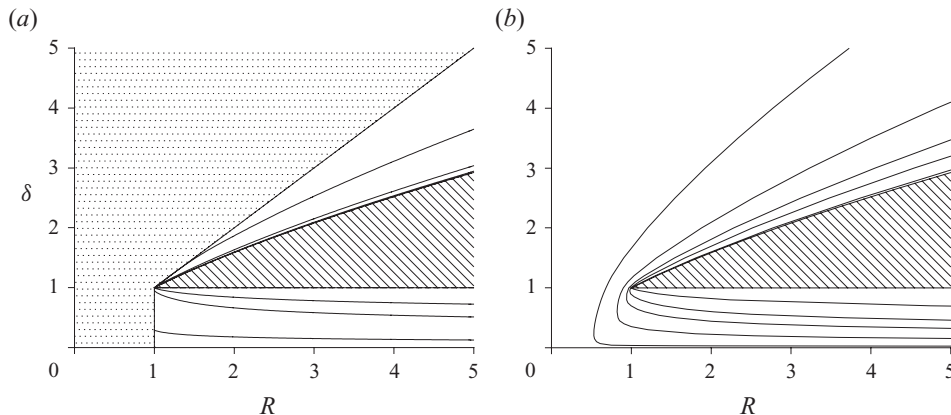


FIGURE 11. In (a) neutral stability curves are illustrated at the times $t_0 = 0, 10^3, 10^6, 10^9$ and ∞ , and in (b) contours of t_σ are illustrated at the times $10^3, 10^4, 10^5, 10^6, 10^9$ and ∞ in the (R, δ) plane. In (a) the dotted zone indicates the region which is already unstable at $t_0 = 0$ while the dashed zone indicates the region which remains stable for all time.

4.5. Discussion

Finally, in order to understand the behaviour throughout the (R, δ) plane, the neutral stability curves are illustrated in figure 11(a) at $t_0 = 0$ and $t_0 = 10^n$ for $n = 3-9$ in uniform increments of 3. For $\delta \geq 1$, figure 11(a) illustrates that the neutral stability curve for the DD instability is located at $\delta = R$. As time goes by, the DDD instability takes place in the $R > 1, \delta > 1$ zone, and the neutral stability curve expands in time from $\delta = R$ to $\delta = R^{2/3}$, which confirms the large-time asymptotic prediction. In the large-time asymptotic limit, for $\delta < 1$, we find that the onset wavenumber scales like $t_0^{-1/2}$ and, on the neutral stability curve, R is found to be approximately proportional to $\delta^{3/2} [\sqrt{t_0}(1 + \delta)/(1 - \delta)]^{\delta^{-1}-1}$, where t_0 is the onset time.

For $\delta < 1$, a DLC instability appears in the region $R > 1$. The unstable region is initially located near $R = 1$ and $\delta = 0$; however, as time increases, the unstable region slowly expands to eventually encompass the whole $\delta < 1$ for $R > 1$ region. Together the DD, DDD and DLC instabilities destabilize most of the (R, δ) parameter space at $t_0 \rightarrow \infty$, just leaving the stable region $R^{2/3} > \delta > 1$.

Further, in figure 11(b), contours of t_σ are illustrated for $t_\sigma = 10^n$ for $n = 3, 4, 5, 6$ and 9. Interestingly, the contours of t_σ , which can be thought of as a measure of how unstable the system is to disturbances, reveal that by either increasing or decreasing δ approximately from the line $\delta = R^2$ for $R < 1$, the system becomes more unstable. However, increasing R at any fixed δ always has a stabilizing affect.

5. Nonlinear simulations

To gain insight into the nonlinear dynamics of the various RT, DD, DDD and DLC instabilities and to understand to what extent the results of the time-dependent LSA described in §3, can be useful, we perform nonlinear simulations. System (3.1) is numerically solved in two dimensions by the pseudospectral scheme proposed by Tan & Homsy (1988), which has been adapted to take into account the presence of two diffusing species. In the initial condition, the concentrations of the species are given by a step function with the addition of a small amount of noise in order to trigger the emergence of the instability in a reasonable computing time. The results

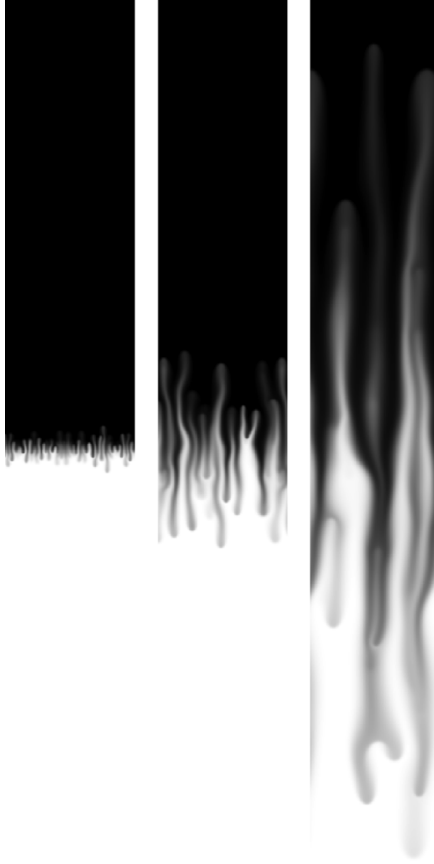


FIGURE 12. DD instability for $(R, \delta) = (1.083, 3)$, concentration maps of species A at times $2.5 \times 10^4, 10^5, 4.4 \times 10^5$. $L_x = 6 \times 10^4$.

are shown as 2-D concentration maps on a grey-scale between 0 (white) and 1 (black) on a finite dimensionless domain of length L_x and width L_y . In the captions we only specify the value of L_x , as the value of L_y is fixed by the aspect ratio of the image.

We start by looking at DD dynamics under conditions for which the system is readily unstable at $t = 0$, i.e. in a case when $\delta > R > 1$. Specifically, we take $R = 1.083$, $\delta = 3$ (figure 12), which corresponds to the experimental situation studied by Pringle & Glass (2002) in a Hele-Shaw cell with sucrose (here A in black in figure 12) on top of a miscible, denser solution of the faster diffusing salt (here B). The nonlinear dynamics of A compare favourably with the corresponding experimental results in figure 8 of Pringle & Glass (2002). The concentration map of B (not shown) is similar, but complementary with a smoother contrast, as B diffuses faster than A. As in the experiments, the fingers extend symmetrically towards the top and the bottom with respect to the position of the initial interface.

As the base-state concentration profiles are error functions which are antisymmetric and because of the particular form of the equations, this problem has a symmetry about $x = 0$. Indeed, one can write the dimensional concentrations as $A = A_0/2 + \tilde{A}(x)$ and $B = B_0/2 + \tilde{B}(x)$, with $\tilde{A}(-x) = -\tilde{A}(x)$ and $\tilde{B}(-x) = -\tilde{B}(x)$. System (3.1) is invariant under the transformation $x \rightarrow -x$, $\Psi \rightarrow -\Psi$, $A \rightarrow 1 - A$ and $B \rightarrow 1 - B$.

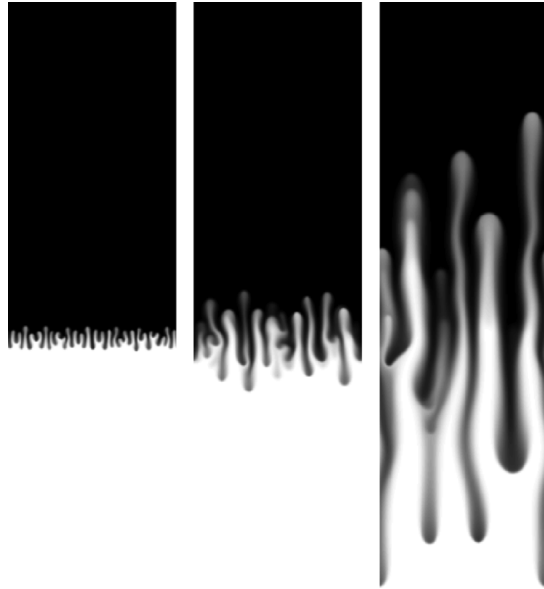


FIGURE 13. RT instability for $(R, \delta) = (0.5, 1)$, concentration maps of species A at times 10^4 , 3×10^4 , 9×10^4 . $L_x = 2^{15}$.

This implies that convective patterns in porous media evolve the same way on both sides of the initial interface.

The same symmetry exists if $R < 1$ for RT patterns in porous media and Hele-Shaw cells (Wooding 1969; Manickam & Homsy 1995; Fernandez *et al.* 2002), as seen in figure 13. Let us note that, for $R < 1$, the line $\delta = 1$ is a special case. Indeed, since the diffusion coefficients are then the same, the problem reduces to that of a single species RT problem, contributing to density as $\alpha_A A + \alpha_B B = \alpha_B B_0 + \alpha_A A(1 - R)$. The lengths and time then rescale like $(1 - R)$ and $(1 - R)^2$, respectively. Thus, on the line $\delta = 1$, only one simulation like that of figure 13 is sufficient to encompass the dynamics which is self-similar in R . When A and B have the same diffusion coefficient, the concentration map of B is the exact complementary of the concentration map of A and the pattern of the total density is the same as the pattern of A.

One can see that the patterns are quite similar for DD finger convection (figure 12) ($\delta > R > 1$) and for pure RT instability (figure 13) ($\delta = 1$, $R < 1$). This comes from the similarity in the eigenfunctions, as described in the previous section. In both cases their maxima are located around the initial position of the interface at $x = 0$ (see figure 5b).

The eigenfunctions are quite different in the case of DLC, as seen in figure 10, which shows that the instability is expected to develop independently in layers above and below the contact line. This is confirmed from figure 14, which shows the DLC pattern soon after the beginning of the nonlinear regime. Convection takes place on both sides of the initial contact line but not around it. Moreover, the pattern on top develops independently of the one on the bottom. This is confirmed by a close inspection of the stream function which shows that the vortices on top are independent of those on the bottom. Here B has a sharper contrast than A as $\delta < 1$. The density map confirms the origin of the DLC mechanism: a depleted zone low in density (here in white) develops above the interface while an accumulation zone where the density is maximum (in black) is obtained below the interface.

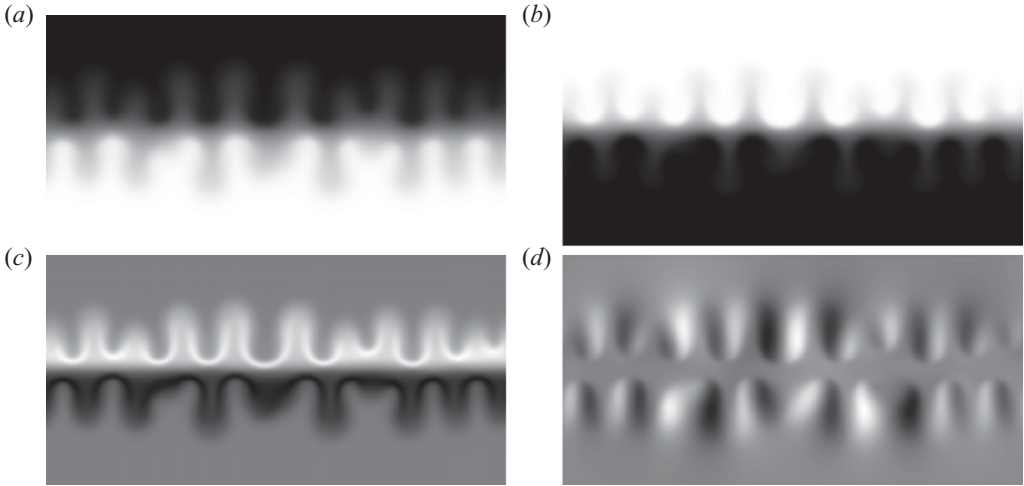


FIGURE 14. DLC instability for $(R, \delta) = (1, 0.3)$, concentration maps of species (a) A and (b) B at time 10^4 . Scale between 0 (white) and 1 (black) and $L_x = 4000$. (c) Corresponding density map between 0.85 (white) and 1.15 (black). (d) Stream function amplitude between -10 and 10 .

5.1. Influence of δ in the RT regime

Experiments on the RT instability are usually performed for a fixed set of solutes in varying concentrations, i.e. fixed δ and variable R . It is then known that decreasing R enhances the instability, as can be seen, for example, at $t=0$ for $\delta=1$ from (3.13). Much less understood is the influence of differential diffusion of the two species at fixed R , for $\delta \neq 1$. Figure 15 compares the nonlinear dynamics in the RT regime at fixed $R=0.5$ but variable δ . In agreement with the LSA (figure 3b), an increase of δ increases the RT destabilization provided $\delta > R^2$ and correspondingly, as seen in figure 15, the wavelength decreases and the fingers extend further away at the same time. This is also seen in figure 16, which shows the temporal evolution of the mixing length (defined as the distance between $\langle A \rangle = 0.01$ and 0.99 where $\langle \cdot \rangle$ stands for an average of the concentration along the transverse direction y). At early times, i.e. before the instability sets in, a diffusive behaviour in which the mixing length grows as $t^{0.5}$ is observed. Once the instability develops, the growth of the mixing length is larger than $t^{0.5}$ and, for a fixed early time, the slope of this growth increases for increasing δ . At later times, however, the asymptotic mixing velocities are all similar, irrespective of the value of δ . The same trend would be observed if δ is decreased below R^2 . Note that the mixing length is difficult to measure when $\delta \rightarrow 0$ because infinitesimally small time steps are then needed for the integration.

As already discussed by Shirtcliffe and coworkers (Shirtcliffe 1973; Linden & Shirtcliffe 1978), one could also measure a dimensionless flux defined as the flux of A versus the flux of B across the position of the initial contact line which, in the diffusive regime, evolves as the square root of the diffusion coefficient ratio. However, in the nonlinear regime, it is quite difficult to estimate the value of the dimensionless flux. Indeed, looking at the patterns obtained by nonlinear simulations it is obvious that the flux along one vertical line will vary in time because of convection and will, moreover, depend on the position of this line. One quantity that would make sense to follow in time would be the mean flux obtained by averaging the flux along the transverse coordinate. Even in that case, one would, in addition, need to make ensemble average of this mean flux on several simulations made for a single set of

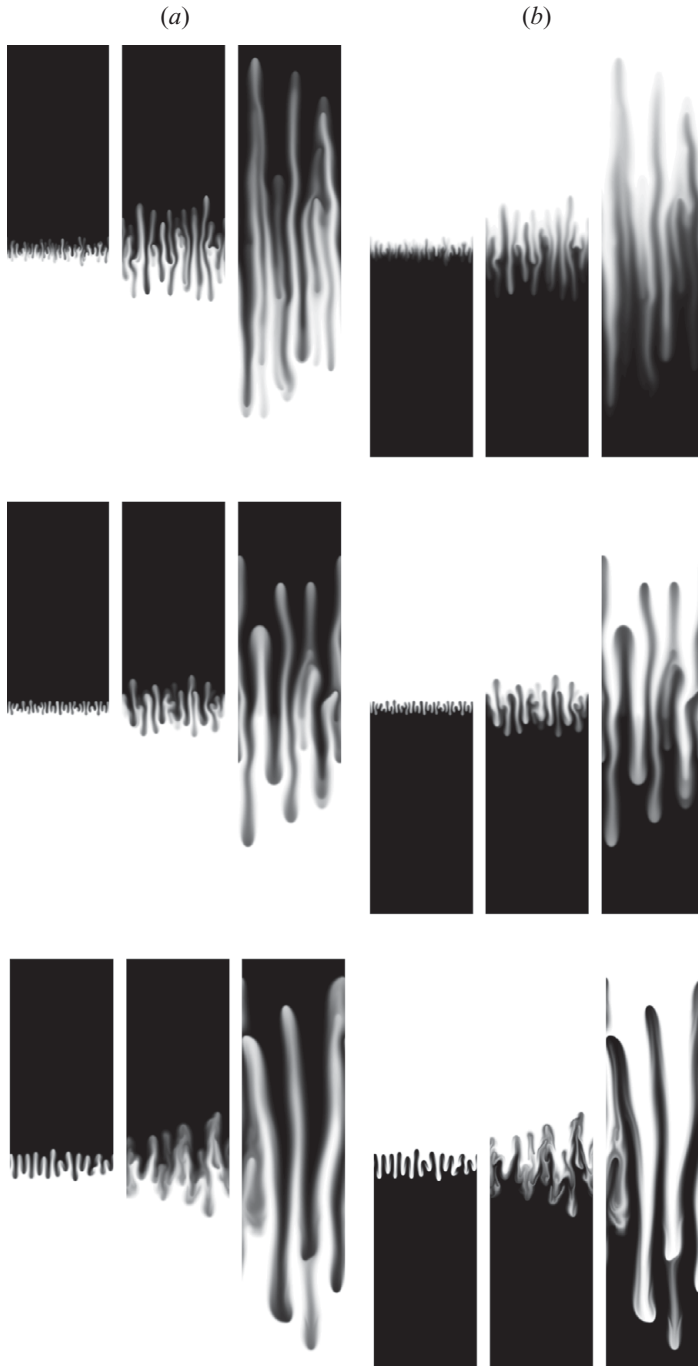


FIGURE 15. Concentration maps of species (a) A and (b) B for $R=0.5$. $L_x = 32000$. (Top) $\delta = 3$ at times 10^4 , 3×10^4 , 9×10^4 ; (middle) $\delta = 1$ at times 10^4 , 3×10^4 , 9×10^4 ; (bottom) $\delta = 0.3$ at times 2×10^4 , 5×10^4 , 1.3×10^5 .

parameters but different noise seeding the initial condition (De Wit, Bertho, Martin 2005). To perform a parametric study of the scalings of such statistical ensemble averages of mean fluxes is beyond the scope of the present paper. It might, however,

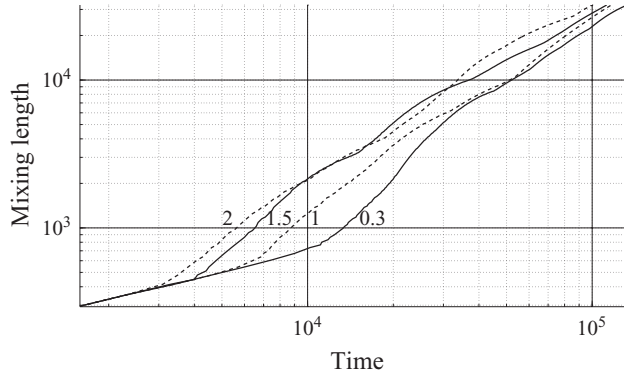


FIGURE 16. Mixing length as a function of time for the RT instability with $R = 0.5$ and δ between 0.3 and 2.

be interesting to perform such measurements in future numerical and experimental studies.

The bottom of figure 15 shows that, when $\delta < 1$, the concentration field of B has a sharper contrast than that of A because B diffuses more slowly. Moreover, differential diffusion of the two species leads to fingers with mushroom-type heads. This results from the fact that, as the lighter B on the bottom diffuses more slowly than A, a layer of less dense fluid forms by diffusion around the heavy falling fingers but this less dense layer is surrounded by a denser layer. The less dense layer is due to a depletion of A as it diffuses out of the fingers faster than B diffuses in. The outer surrounding denser layer is due to the formation of a zone where both A and B have diffused to result in a layer denser than its surroundings. The layers of various relative densities affect the flow field and result in the formation of the mushroom structures.

5.2. Transition from the RT to the DD regime

Figure 17 examines the transition from RT to DD instabilities when δ is fixed at 3 and R is progressively increased. As A diffuses more slowly than B, its concentration map has a sharper contrast than that of B. As explained earlier, the patterns look alike in both RT ($R < 1$) and DD mechanisms ($R > 1$). Increasing R has a stabilizing effect as the destabilizing density ratio is then decreasing. This is confirmed by figure 18(a) where the mixing lengths depart later and, at a fixed time, reach smaller values when R increases. The asymptotic mixing velocities also decrease when R increases. Above a critical value of R , which is an increasing function of δ (see figure 11), the system is stabilized as DD effects are no longer strong enough to destabilize the stratification of A on top of denser B. As anticipated from the LSA (see figure 3a), the transition between RT and DD is quantitatively smooth.

5.3. Transition from the RT to the DLC regime

To see how the pattern changes between the RT and DLC instabilities, let us now fix $\delta = 0.3$ and increase R (see figure 19). In the RT regime ($R < 1$), fingers extend symmetrically around the interface but mushrooms are observed in B as $\delta < 1$. Once $R > 1$, the DLC mechanism becomes operational, characterized by two sets of vortices developing at equal distance from the interface, one above and one below it. It is interesting to note that, for $R = 0.7$, the stream function field shows a DLC structure at early times before fingers extending across the interface take over at longer times. As R is increased, the intensity of the flow decreases, as can be seen from the mixing

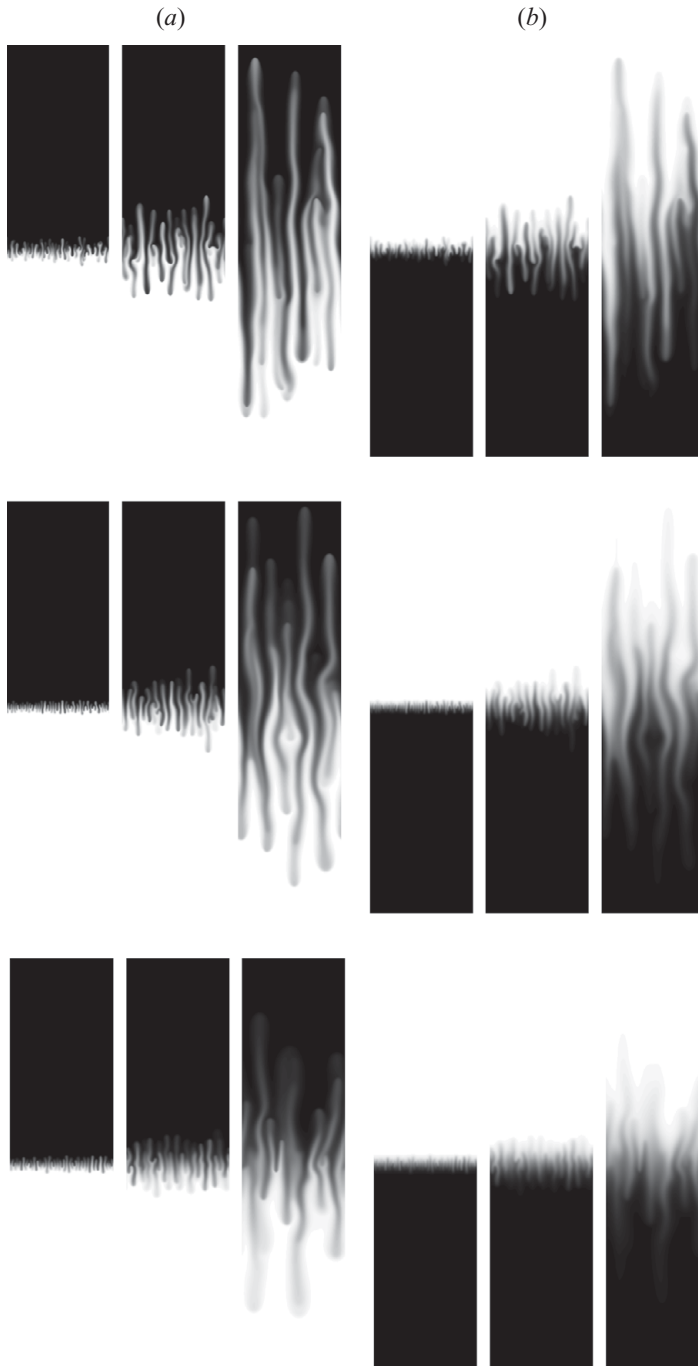


FIGURE 17. Concentration maps of species (a) A and (b) B for $\delta = 3$, $L_x = 32000$. (Top) $R = 0.5$ at times 10^4 , 3×10^4 , 9×10^4 ; (middle) $R = 1$ at times 10^4 , 4×10^4 , 1.9×10^5 ; (bottom) $R = 1.5$ at times 2×10^4 , 8×10^4 , 3.5×10^5 .

length (figure 18b), and the instability starts later. The transition between the RT and DLC regimes is more abrupt in terms of mixing lengths because of a profound change in the nature of the flow field and also because the DLC starts much later.

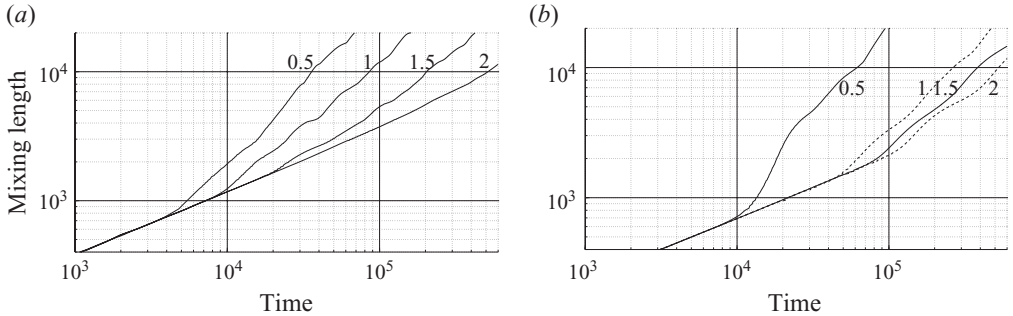


FIGURE 18. Mixing length as a function of time for variable values of R indicated on the curves and (a) $\delta = 3$. The transition between RT and DD instabilities occurs smoothly with a progressive stabilization as R increases. (b) $\delta = 0.3$. The transition between RT and DLC instabilities occurs more abruptly.

We end this section by noting that the mechanisms of instabilities described here will be the same in three dimensions as they are related to the properties of the density profile along the 1-D gravity direction. However, quantitative changes in the stability properties and nonlinear simulations are to be expected in thicker Hele-Shaw cells when Darcy's law is no longer valid and must be replaced by Navier–Stokes equations (Martin *et al.* 2002).

6. Conclusions

In the gravity field, buoyancy-driven convection can appear when two solutions containing different species, say A on top of B, are put in contact along a horizontal line. Once the solutes start to diffuse their concentration profiles evolve, leading to a time-dependent density profile. The goal of this paper was to examine the various buoyancy-driven instabilities that can occur in porous media or Hele-Shaw cells and to classify them in a parameter space spanned by the buoyancy ratio R , quantifying the contribution to the density of B over that of A, and the diffusion coefficient ratio $\delta = D_B/D_A$ of the two species. Using a QSSA, an LSA of time-dependent base-state density profiles shows that the stability boundaries depend on time. Numerical simulations of the full nonlinear problem further highlight the properties of the various possible convective regimes.

At $t = 0$ and for $R < 1$, i.e. a statically unstable stratification of a denser solution of A on top of a less dense solution of B, the system is, as expected, readily unstable at the moment of contact because of an RT instability. In particular, in this case we examine the influence of differential diffusion between the two species, and show that the system is more unstable when species B in the lighter solution on the bottom diffuses faster than A on the top ($\delta > 1$). On the contrary, when B diffuses more slowly ($\delta < 1$), the system is less unstable and favours fingers with mushroom-shaped heads in the nonlinear regime. For $R > 1$, i.e. in the case of a given solution of A on top of a denser solution of B, the system is also immediately unstable at $t = 0$ with a DD instability provided the component B in the denser solution on the bottom diffuses sufficiently faster, in effect if $\delta > R$.

At later times, a larger part of the (R, δ) parameter plane is destabilized as well. If B diffuses faster, the DD instability zone further expands in time below the $\delta > R$ curve. This additional zone of instability due to a DDD mechanism then extends up to the $\delta = R^{2/3}$ curve below which the system remains stable in the $\delta > 1$ zone

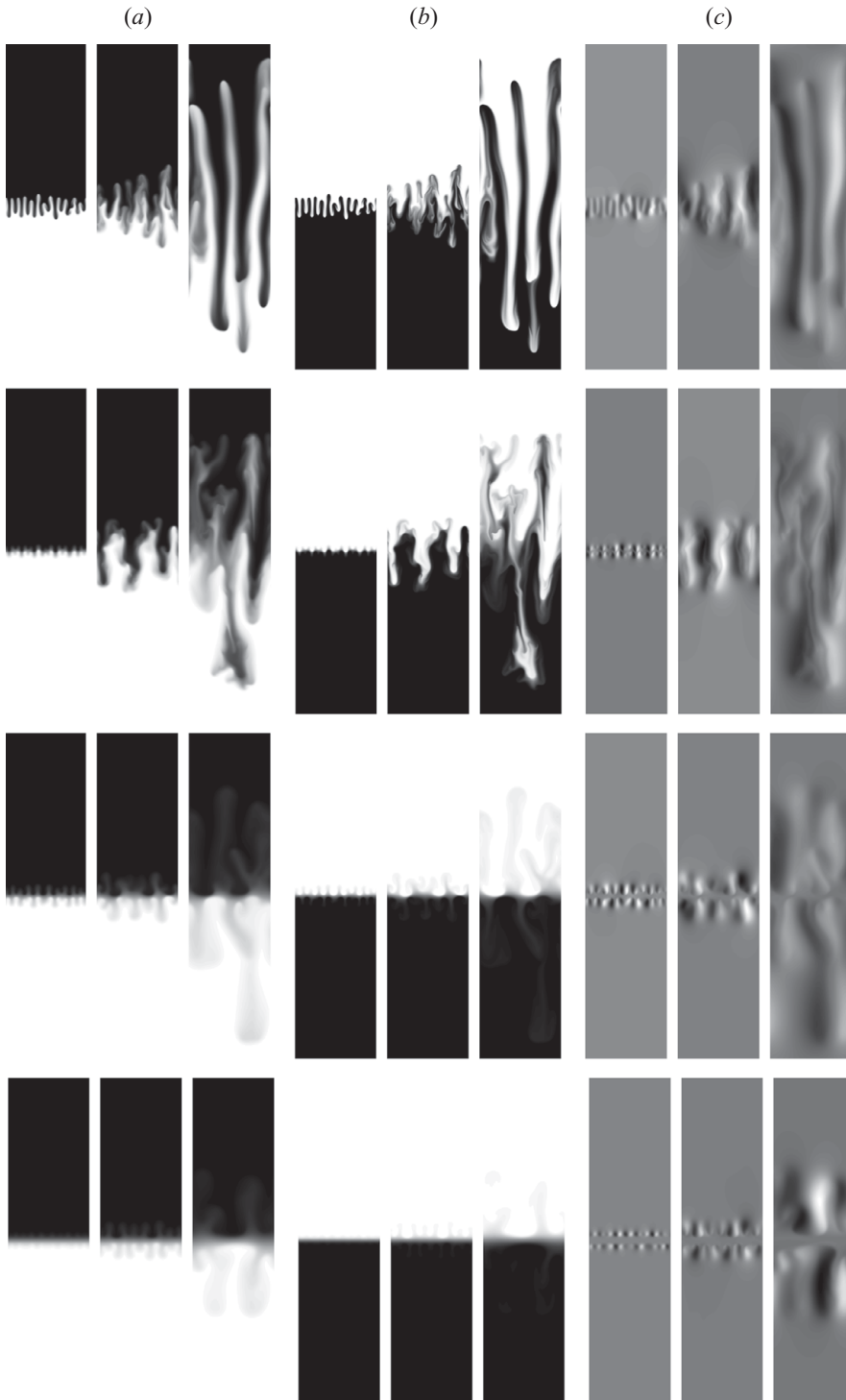


FIGURE 19. Concentration maps of species (a) A, (b) B and (c) stream function ψ for $\delta = 0.3$. $L_x = 32000$. (First line) $R = 0.5$ at times 2×10^4 , 5×10^4 , 1.3×10^5 ; (second line) $R = 0.7$ at times 3×10^4 , 10×10^4 , 2.5×10^5 ; (third line) $R = 1$ at times 7×10^4 , 1.5×10^5 , 5.9×10^5 ; (fourth line) $R = 1.5$ at times 7×10^4 , 1.5×10^5 , 5.9×10^5 .

(see figure 11). This large-time asymptotic neutral stability curve associated with the DDD instability is the same as that obtained in the limit of linear constant base-state profiles. In the nonlinear regime, the DD and DDD patterns bear strong similarities with RT fingers, i.e. convective deformations extend symmetrically above and below the initial line of contact, the most unstable zone being located on the interface. At fixed $\delta > 1$, both the intensity of convection and the extent of the fingering zone then decrease smoothly when R is increased.

Time-dependent stability analysis further shows destabilization in time of the zone $R > 1 > \delta$ classically stable if the LSA is performed using linear profiles. This corresponds to the situation of a less dense solution on top of a denser one, the fastest diffusing species now being placed on the top. Instabilities then occur due to a DLC mechanism providing accumulation in time of the fast diffusing species in the bottom layer and its depletion in the upper one. The resulting non-monotonic density profiles trigger convection in two zones positioned at symmetric distances above and below the initial contact line. Nonlinear simulations confirm this trend with the intensity of convection and the length of the mixing zone decreasing when R increases at fixed $\delta < 1$.

Nonlinear simulations are in good agreement with experiments performed in Hele-Shaw cells in the RT (Fernandez *et al.* 2002), DD (Cooper *et al.* 1997; Pringle & Glass 2002) and DLC regimes (Griffiths 1981). We hope that the present classification will trigger more systematic experimental work devoted to quantifying the transitions from one type of instability to another. This can be achieved by varying the buoyancy ratio R at fixed δ by adjusting the relative concentrations of a fixed pair of species A and B. Using sugar and salt, for instance, where $\delta \sim 3$ transitions between RT, DD (much like in figures 17 and 18a) and even DDD mechanisms can be done by varying concentrations of sugar on top of salt. On the other hand, the reverse case of salt on top of sugar at $\delta \sim 0.3$ allows us to investigate transitions from RT towards DLC when R is increased. In the same line, transitions at fixed R but varying δ can be obtained by appropriately choosing concentrations of different species of varying diffusion coefficients.

This paper is dedicated to A. Zebib whose friendship and fruitful advice will be greatly missed. We acknowledge Prodex (Belgium) and FNRS for financial support.

REFERENCES

- ALMARCHA, C., TREVELYAN, P. M. J., GROSFILS, P. & DE WIT, A. 2010a Chemically driven hydrodynamic instabilities. *Phys. Rev. Lett.* **104**, 044501.
- ALMARCHA, C., TREVELYAN, P. M. J., RIOLFO, L. A., ZALTS, A., EL HASI, C., D'ONOFRIO, A. & DE WIT, A. 2010b Active role of a color indicator in buoyancy-driven instabilities of chemical fronts. *J. Phys. Chem. Lett.* **1**, 752–757.
- COOPER, C. A., GLASS, R. J. & TYLER, S. W. 1997 Experimental investigation of the stability boundary for double-diffusive finger convection in a Hele-Shaw cell. *Water Resour. Res.* **33**, 517–526.
- DE WIT, A. 2001 Fingering of chemical fronts in porous media. *Phys. Rev. Lett.* **87**, 054502.
- DE WIT, A., BERTHO, Y. & MARTIN, M. 2005 Viscous fingering of miscible slices. *Phys. Fluids* **17**, 054114.
- D'HERONCOURT, J., DE WIT, A. & ZEBIB, A. 2007 Double-diffusive instabilities of autocatalytic chemical fronts. *J. Fluid Mech.* **576**, 445–456.
- D'HERONCOURT, J., ZEBIB, A. & DE WIT, A. 2006 Reaction driven convection around a stably stratified chemical front. *Phys. Rev. Lett.* **96**, 154501.

- FERNANDEZ, J., KUROWSKI, P., PETITJEANS, P. & MEIBURG, E. 2002 Density-driven unstable flows of miscible fluids in a Hele-Shaw cell. *J. Fluid Mech.* **451**, 239–260.
- GRIFFITHS, R. W. 1981 Layered double-diffusive convection in porous media. *J. Fluid Mech.* **102**, 221–248.
- HUPPERT, H. E. & MANINS P. C. 1973 Limiting conditions for salt-fingering at an interface. *Deep Sea Res.* **20** 315–323.
- HUPPERT, H. E. & TURNER, J. S. 1981 Double diffusive convection. *J. Fluid Mech.* **106**, 299–329.
- KALLIADASIS, S., YANG, J. & DE WIT, A. 2004 Fingering instabilities of exothermic reaction–diffusion fronts in porous media. *Phys. Fluids* **16**, 1395–1409.
- KUNZE, E. 2003 A review of oceanic salt-fingering theory. *Prog. Oceanogr.* **56**, 399–417.
- LINDEN, P. F. & SHIRTCLIFFE, T. G. L. 1978 The diffusive interface in double diffusive convection. *J. Fluid Mech.* **87**, 417–432.
- MANICKAM, O. & HOMS, G. M. 1995 Fingering instabilities in vertical miscible displacement flows in porous media. *J. Fluid Mech.* **288**, 75–102.
- MARTIN, J., RAKOTOMALALA, N. & SALIN, D. 2002 Gravitational instability of miscible fluids in a Hele-Shaw cell. *Phys. Fluids* **14**, 902–905.
- NIELD, D. A. 1968 Onset of thermohaline convection in a porous medium. *Water Resour. Res.* **4**, 553–560.
- NIELD, D. A. & BEJAN, A. 2006 *Convection in Porous Media*. Springer.
- PRINGLE, S. E. & GLASS, R. J. 2002 Double-diffusive finger convection: influence of concentration at fixed buoyancy ratio. *J. Fluid Mech.* **462**, 161–183.
- PRITCHARD, D. 2009 The linear stability of double-diffusive miscible rectilinear displacements in a Hele-Shaw cell. *Eur. J. Mech. B/Fluids* **28**, 564–577.
- SASAKI, S. 1996 Development of coupled molecular diffusion to convective fingering. *J. Phys. Chem.* **100**, 20164–20171.
- SCHMITT, R. W. 2003 Observational and laboratory insights into salt finger convection. *Prog. Oceanogr.* **56**, 419–433.
- SHIRTCLIFFE, T. G. L. 1973 Transport and profile measurements of the diffusive interface in double diffusive convection with similar diffusivities. *J. Fluid Mech.* **57**, 27–43.
- STAMP, A. P., HUGHES, G. O., NOKES, R. I. & GRIFFITHS, R. W. 1998 The coupling of waves and convection. *J. Fluid Mech.* **372**, 231–271.
- STERN, M. E. 1960 The salt-fountain and thermohaline convection. *Tellus* **12**, 172–175.
- STERN, M. E. & TURNER, J. S. 1969 Salt fingers and convective layers. *Deep Sea Res.* **16**, 497–511.
- STOMMEL, H., ARONS, A. B. & BLANCHARD, D. 1956 An oceanographic curiosity: the perpetual salt fountain. *Deep-Sea Res.* **3**, 152–153.
- TAN, C. T. & HOMS, G. M. 1986 Stability of miscible displacements in porous media: rectilinear flow. *Phys. Fluids* **29**, 3549–3556.
- TAN, C. T. & HOMS, G. M. 1988 Simulation of nonlinear viscous fingering in miscible displacement. *Phys. Fluids* **31**, 1330–1338.
- TURNER, J. S. 1979 *Buoyancy Effects in Fluids*. Cambridge University Press.
- TURNER, J. S. & CHEN, C. F. 1974 Two-dimensional effects in double diffusive convection. *J. Fluid Mech.* **63**, 577–592.
- TURNER, J. S. & STOMMEL, H. 1964 A new case of convection in the presence of combined vertical salinity and temperature gradients. *Proc. Natl Acad. Sci. USA* **52**, 49–53.
- WOODING, R. A. 1969 Growth of fingers at an unstable diffusing interface in a porous medium or Hele-Shaw cell. *J. Fluid Mech.* **39**, 477–495.
- ZALTS, A., EL HASI, C., RUBIO, D., URENA, A. & D’ONOFRIO, A. 2008 Pattern formation driven by an acid–base neutralization reaction in aqueous media in a gravitational field. *Phys. Rev. E* **77**, 015304.